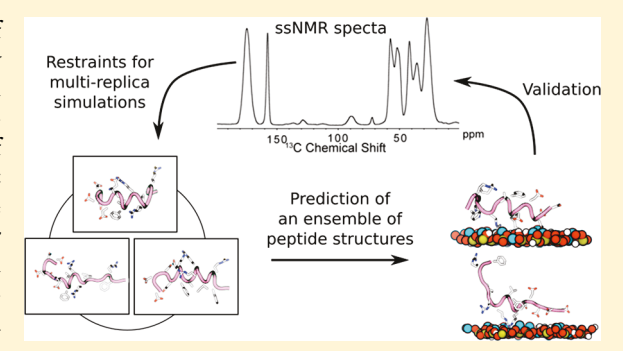


Solid-State NMR and MD Study of the Structure of the Statherin Mutant SNa15 on Mineral Surfaces

Erika L. Buckle, †,+ Arushi Prakash, ‡,+ Massimiliano Bonomi, § Janani Sampath, ‡ Jim Pfaendtner, *,‡ and Gary P. Drobny*, †

Supporting Information

ABSTRACT: Elucidation of the structure and interactions of proteins at native mineral interfaces is key to understanding how biological systems regulate the formation of hard tissue structures. In addition, understanding how these same proteins interact with nonnative mineral surfaces has important implications for the design of medical and dental implants, chromatographic supports, diagnostic tools, and a host of other applications. Here, we combine solid-state NMR spectroscopy, isotherm measurements, and molecular dynamics simulations to study how SNa15, a peptide derived from the hydroxyapatite (HAP) recognition domain of the biomineralization protein statherin, interacts with HAP, silica (SiO₂), and titania (TiO₂) mineral surfaces. Adsorption isotherms are used to



characterize the binding affinity of SNa15 to HAP, SiO₂, and TiO₂. We also apply 1D ¹³C CP MAS, 1D ¹⁵N CP MAS, and 2D ¹³C-¹³C DARR experiments to SNa15 samples with uniformly ¹³C- and ¹⁵N-enriched residues to determine backbone and side-chain chemical shifts. Different computational tools, namely TALOS-N and molecular dynamics simulations, are used to deduce secondary structure from backbone and side-chain chemical shift data. Our results show that SNa15 adopts an α -helical conformation when adsorbed to HAP and TiO2, but the helix largely unravels upon adsorption to SiO2. Interactions with HAP are mediated in general by acidic and some basic amino acids, although the specific amino acids involved in direct surface interaction vary with surface. The integrated experimental and computational approach used in this study is able to provide high-resolution insights into adsorption of proteins on interfaces.

INTRODUCTION

Several organisms produce hard structures such as bone, teeth, shells, and exoskeletons from inorganic materials (i.e., calcite, silica, and hydroxyapatite) through a process known as biomineralization. These organisms use specialized proteins that interact with these inorganic materials thereby accelerating1 or inhibiting2,3 the growth of mineral solids, or even altering mineral morphology. 4-10 Detailed atomic-level insight of how of proteins interact with these minerals is required to better understand the role that proteins play in biomineralization and to thereafter exploit it for materials synthesis. This requires the resolution of the secondary and tertiary structure of proteins adsorbed on surfaces, the identification of both the residues that are crucial for protein-surface interaction and the nature of protein-surface interactions.

To date, only a handful of experimentally confirmed structural models of proteins interacting with their native mineral surfaces have been reported. These protein surface systems include either small extracellular matrix (ECM) proteins or ECM protein domains that are adsorbed onto hydroxyapatite (HAP) crystals. 19-30 These studies

suggest that protein secondary structure can change when adsorbed to surfaces. They also hypothesize that the interaction of amino acid side-chains with inorganic surfaces are dependent on the secondary structures of adsorbed proteins. 21,24,26,28,31,32 Thus, all components of protein surface interaction can be determined only when the structure of the adsorbed protein is resolved.

Salivary statherin is a 43-residue ECM protein (DpSpS-EEKFLRRIGRFGYGYGPYQPVPEQPLYPQPYQPQ-YQQYTF) that regulates HAP nucleation at enamel surfaces. The structure of statherin adsorbed onto HAP has been resolved.^{30,33-35} Statherin has been studied by calorimetric methods, ^{12,25} adsorption isotherms, ^{33,36} solution NMR, ^{37,38} solid-state NMR (ssNMR), ^{20–22,24,25,27,28,30,34,35,39,40} and circular dichroism. 33,41 These studies indicate that statherin is unstructured in solution but structures when adsorbed onto HAP surfaces. Notably, the 15-residue long N-terminus adopts

Received: October 11, 2018 Published: January 8, 2019

1998

Department of Chemistry, University of Washington, Box 351700, Seattle, Washington 98195, United States

[‡]Department of Chemical Engineering, University of Washington, Seattle, Washington 98195, United States

[§]Structural Bioinformatics Unit, Institut Pasteur, CNRS UMR 3528, 75015 Paris, France

a distorted α -helical conformation, and the C-terminus also becomes partly helical upon adsorption to HAP. 35,42,43

These studies also identify specific residues in statherin that interact with HAP. For example, acidic side-chains exhibit strong affinity for calcium phosphate surfaces. 33 Consequently, the N-terminus of statherin, which contains acidic residues like phosphoserine (pS), aspartic acid (D), and glutamic acid (E), has been shown to be essential for HAP binding.³³ Similarly, the interaction of basic residues with HAP have also been studied. When Goobes et al. mutated selected basic residues to alanine, the protein displayed a lower binding affinity to the surface, but the surface coverage or adsorption enthalpy was not affected.³⁰ In contrast, when all the basic residues (K6, R9, R10. and R13) were replaced with alanine, there was a significant change in the adsorption enthalpy and surface coverage. Therefore, they hypothesized that the nature of basic residues is not as important to binding as the presence of a number of basic residues.³⁰ In contrast to acidic and basic residues, the role of nonpolar residues in protein-surface interactions is less clear. The HAP-binding domain of statherin has four types of nonpolar residues (L, I, G, and F) but only F14 was found to be in proximity with the HAP surface. 20,23

There are limited studies that model the interaction of statherin and HAP. Notably, Rosetta and RosettaSurface modeling programs have been used for this. 31,44,45 However, these all-atom models of the protein include simplifying assumptions that make calculations faster, like freezing the surface, restraining the protein backbone, and not accounting for waters and ions. Thus, they might exclude important interactions that affect protein structures. MD simulations, which can explicitly model the surface, protein, and solvent, include these interactions. In fact, recent advances in the use of advanced MD-based simulation methods like metadynamics^{46,47} have been shown to be highly effective in simulating the structure and binding of peptides at surfaces.⁴⁸ Furthermore, owing to the ease with which NMR chemical shifts can be directly estimated from classical simulations, 49,50 the metadynamic metainference approach^{51,52} has been developed as part of a growing integrative structural biological toolkit⁵³ for pairing enhanced sampling MD simulations with experimental structural restraints.

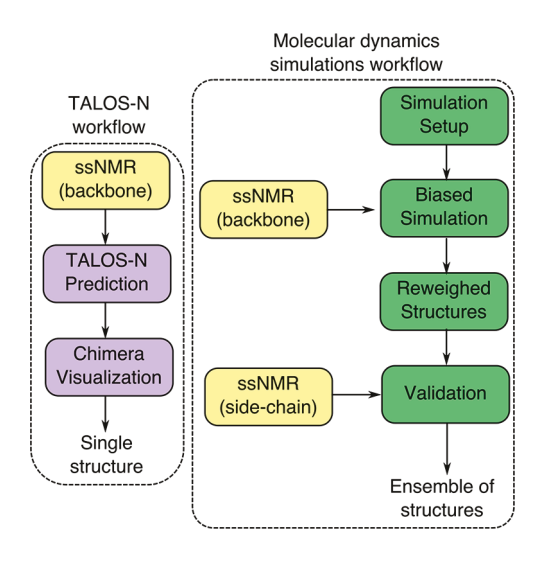
Metainference⁵² is a quantitative and rigorous mathematical framework based on Bayesian inference. In this approach, a structural ensemble of the protein or peptide is generated by a multireplica MD simulation guided by a hybrid energy function, which combines physicochemical information (the atomistic force field) with additional conformational restraints aimed at enforcing agreement of the structural ensemble of the peptide with the available experimental data. Furthermore, to accelerate sampling because structural states might be separated by huge energy barriers, metainference is combined with metadynamics (the Parallel-Bias (PBMetaD) flavor).⁵¹ In this combined approach, an additional, time-dependent bias potential is added to each replica and shared among all of them, in the spirit of the multiple-walkers 4 approach. Metadynamic metainference addresses two of the major challenges in molecular simulations: (1) the limited accuracy of empirical force fields, which is improved by the introduction of experimental information, and (2) the time-scale limitations of standard MD, which is accelerated by the use of PBMetaD.

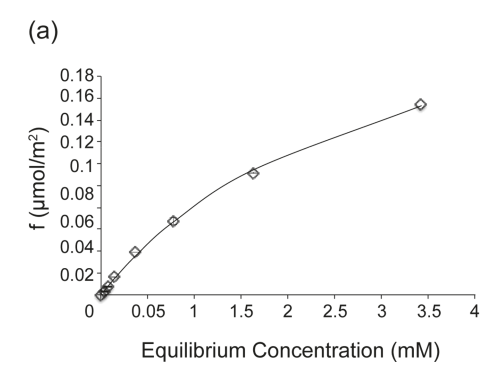
In this study, we make use of the N-terminal domain of statherin, SN15 (DpSpSEEKFLRRIGRFG, where pS indicates a phosphorylated serine), which is often used as a model for

statherin because it has nearly the same binding affinity for HAP as statherin. HAP as statherin. Importantly, the binding of SN15 to HAP is greatly diminished if the serines are not phosphorylated. Remarkably, this binding affinity can be restored when the serine residues are replaced by aspartic acid, leading to the model peptide SNa15 (DDDEEKFLRRIGRFG). We study the adsorption of SNa15 to different inorganic surfaces, namely HAP, silica (SiO₂), and titania (TiO₂). We explore the surface-bound structure of the peptide, identify the binding residues, and investigate the changes in binding upon changing the mineral substrate to which the peptide binds. For this, we use an integrative experimental and simulation approach, similar to recent studies, sepecially using NMR data as structural restraints in the molecular dynamics step to predict binding motifs of peptides on surfaces. S1,56

To characterize binding experimentally, we use both adsorption isotherms and 1D 13C CP MAS, 1D 15N CP MAS, and 2D ¹³C-¹³C DARR experiments. These experiments provide chemical shifts for the backbone and side-chain which can resolve the peptide structure with high fidelity. Further, we use two modeling approaches - TALOS-N and molecular dynamics (MD) simulations. TALOS-N utilizes a protein database to predict the most likely structure of the peptide given the database and the experimentally determined chemical shift data.⁴⁵ However, because peptides often present an equilibrium ensemble of many structures with similar freeenergies, even when bound to a surface, a single snapshot derived from TALOS-N might not provide a complete picture. 52,57 Thus, we use MD simulations with the metadynamic metainference method described above to generate an ensemble of surface-bound conformations consistent with experimental data. This integrated approach allows us to resolve the peptide structure with higher fidelity than possible with a single structure prediction, allowing us to focus on the specificity of the side-chains to the surface. Measured side-chain chemical shifts are not used in the molecular simulation step but kept aside for validation as illustrated in Scheme 1.

Scheme 1. Schematic of the Modeling and Simulation Workflows Used in This Study





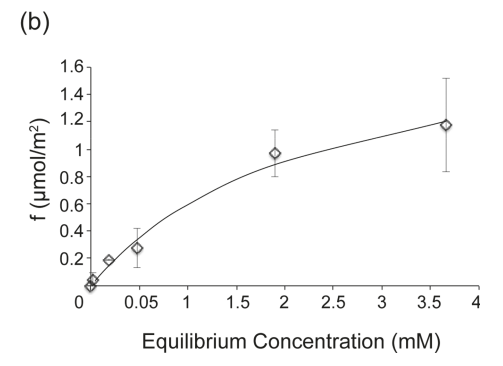


Figure 1. Adsorption isotherms for SNa15 interacting with (a) SiO_2 and (b) TiO_2 . Data are a mean from two independent repeats, and the standard deviation is shown. The disassociation constants obtained from the fitting are $K_d = 2.98$ mM for SiO_2 and $K_d = 2.30$ mM for TiO_2 .

RESULTS

Adsorption Isotherms. To determine how SNa15 interacts with the SiO_2 and TiO_2 surfaces, Langmuir adsorption isotherm curves were measured (Figure 1). Isotherms for SNa15 interacting with HAP can be found in the literature.³³ The curves were fit with eq 1

$$f = A \frac{[\text{SNa15}]}{[\text{SNa15}] + K_{\text{d}}} \tag{1}$$

where K_d is the disassociation constant (mM), f is the fractional saturation, A is a scaling factor (unitless), and [SNa15] is the concentration of free SNa15 in equilibrium (mM). The K_d obtained from these data were 2.98 and 2.30 mM for SNa15 adsorbing onto SiO₂ and TiO₂, respectively. The maximum amounts of SNa15 adsorbed were 0.2 and 1.2 μ mol/m² for SiO₂ and TiO₂, respectively.

Chemical Shift Assignments. To obtain site-specific chemical shift assignments, 1D ¹⁵N CP MAS and 1D ¹³C CP MAS experiments were performed in conjunction with 2D ¹³C-¹³C DARR experiments. We resolved and assigned most of the ¹³C spins and the side-chain ¹⁵N spins in SNa15 containing up to two uniformly ¹³C- and ¹⁵N-enriched amino acids. To assign the chemical shifts for the entire peptide, seven isotopically enriched samples were analyzed, as shown in Table 1. The only amino acids not assigned by this study are L8, I11, and the C-terminal G15.

Table 1. SNa15 Peptides Synthesized in This Study^a

| sample name | label position |
|-------------|-------------------|
| D2R9 | DD*DEEKFLR*RIGRFG |
| D3R10 | DDD*EEKFLRR*IGRFG |
| E4F7 | DDDE*EKF*LRRIGRFG |
| E5F14 | DDDEE*KFLRRIGRF*G |
| К6 | DDDEEK*FLRRIGRFG |
| G12 | DDDEEKFLRRIG*RFG |
| R13 | DDDEEKFLRRIGR*FG |

 $[^]a$ Asterisk indicates that the preceding amino acid is uniformly $^{13}\mathrm{C}$ and $^{15}\mathrm{N}$ enriched.

An example of the data collected for each sample is shown in Figure 2. A 1D ¹⁵N CP MAS (Figure 2a), 1D ¹³C CP MAS (Figure 2b), and 2D ¹³C-¹³C DARR (Figure 2c) spectrum was collected for each sample in order to make complete, unambiguous chemical shift assignments. Because the ¹⁵N amide spins had too much overlap, they could not be assigned

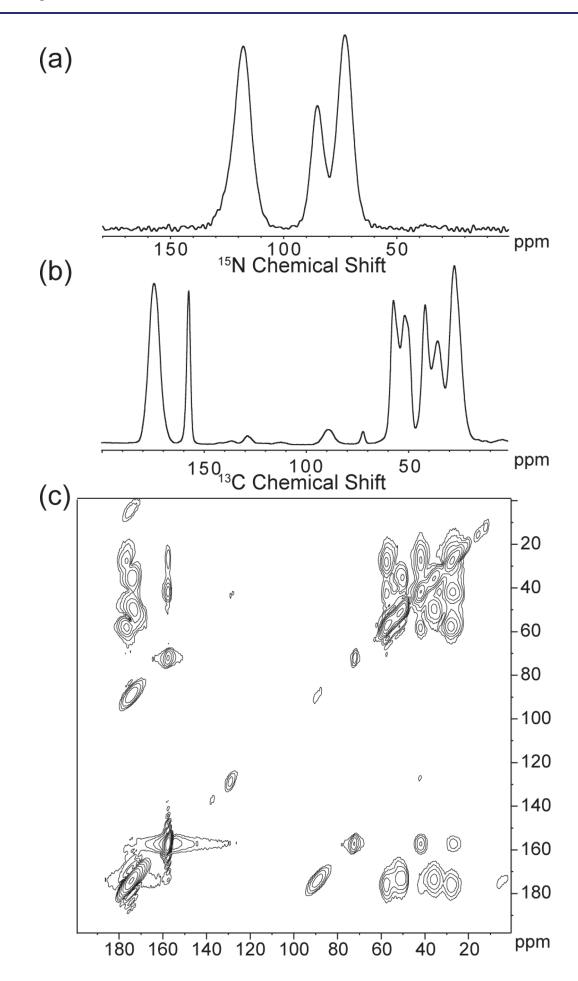


Figure 2. Representative set of the data collected for each labeled SNa15 peptide in each of the studied phases: neat and adsorbed on HAP, SiO_2 , and TiO_2 . The data shown are for D2R9 and are the following: (a) ^{15}N CP MAS, (b) ^{13}C CP MAS, and (c) $^{13}C-^{13}C$ DARR.

unambiguously. Therefore, only the $^{15}\mathrm{N}$ side-chain spins were assigned.

Figure 3 illustrates how all chemical shift assignments are made for the entire neat SNa15 peptide. The cross-peak interactions are highlighted by the dashed red lines and labeled with the corresponding ¹³C spins. These correlations allow for the assignment of unique chemical shifts. All ¹³C chemical shift assignments were made via this method for the entire SNa15 peptide in the four phases studied: neat, adsorbed on HAP, adsorbed on SiO₂, and adsorbed on TiO₂. Because of the

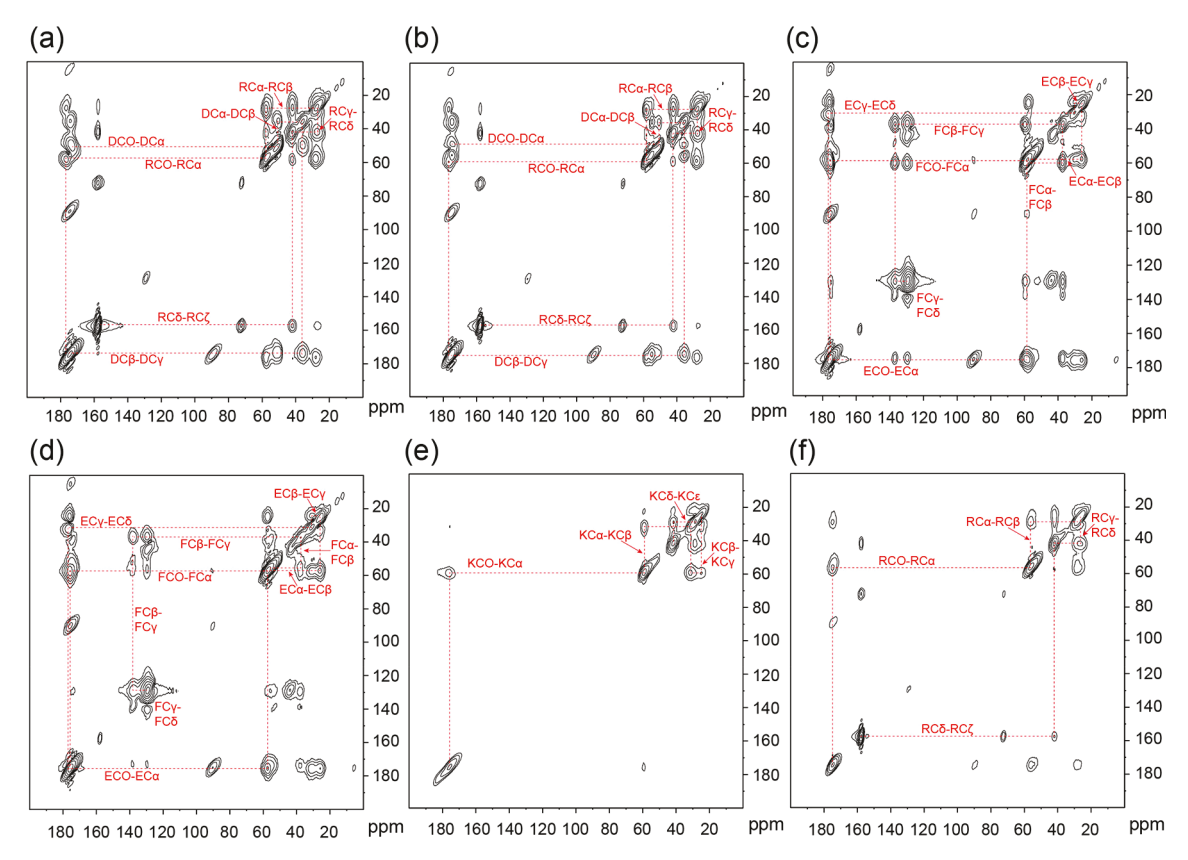


Figure 3. ¹³C-¹³C DARR spectra of neat (a) D2R9, (b) D3R10, (c) E4F7, (d) E5F14, (e) K6, and (f) R13. The dashed lines show the correlation of spins.

broad nature of the ¹³C lineshapes and the overlap in both carbonyl and aliphatic regions, as evident in Figure 2b, 2D spectroscopy was deemed necessary to further resolve these assignments.

Changes in the chemical shifts (Δ CS) of the adsorbed peptide with reference to the peptide in water can provide information about (a) the structural changes of the peptide and (b) changes in local environment upon adsorption of the peptide to the surface. Figure 4 shows the chemical shifts of D2R9 neat and adsorbed to the three inorganic interfaces. The dashed lines emphasize positions of significant differences between these spectra. Notably, the resolution in the aliphatic region significantly decreases upon the adsorption of the peptide, necessitating the use of 2D spectroscopy.

 Δ CS values for the backbone of SNa15 at different surfaces are plotted in Figure 5. These values are obtained by subtracting the chemical shift of the ¹³C spin in neat SNa15 from the corresponding ¹³C spin in the adsorbed SNa15 peptide. A positive Δ CS indicates a downfield perturbation of the chemical shift (higher ppm, less shielded), while a negative Δ CS indicates an upfield perturbation of the chemical shift (lower ppm, more shielded).

From Figure 5, it is evident that some chemical shift trends are common for all three mineral systems. For the case of the Δ CS for ¹³CO, E4 exhibits upfield shifts and G12 exhibits downfield shifts. Similarly, all three adsorbed phases experience large downfield shifts for the ¹³C α spins of G12 and D2. Additionally, they all experience a pronounced downfield shift for the ¹³C β spins of D2 and D3 while there is a pronounced upfield shift for the ¹³C α spins of R13 and the ¹³C β spins of R10. The fact that Δ CS of these residues have the same trend

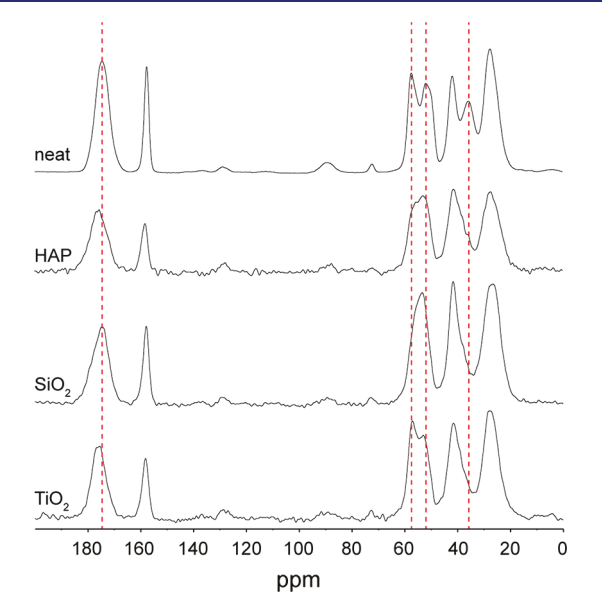


Figure 4. ¹³C CP MAS spectra of D2R9 in four phases: neat, adsorbed to HAP, adsorbed to SiO₂, and adsorbed to TiO₂. The dashed lines highlight some of the more obvious chemical shift differences between the four spectra.

at all interfaces indicates that these regions in the peptide display similar structural changes when adsorbed to any of these surfaces. Specifically, the N-terminus (D2-E4) and the C-terminus (R10, G12, and R13) experience similar conformational changes upon adsorption to HAP, SiO₂, and TiO₂. Additionally, there are pronounced backbone ΔCS changes for

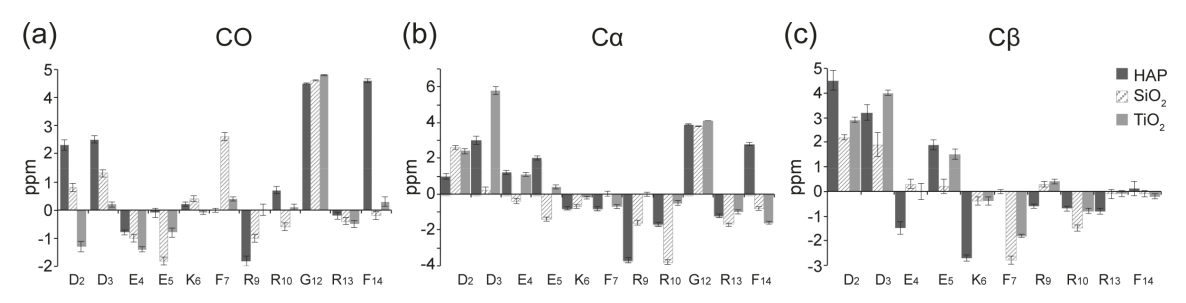


Figure 5. Backbone Δ CS plots showing chemical shift perturbations for (a) 13 CO shifts, (b) 13 C α shifts, and (c) 13 C β shifts. Δ CS for SNa15 on HAP (black), SiO₂ (hatched), and TiO₂ (gray) are in reference to neat SNa15. Positive changes indicate a downfield shift while negative changes indicate an upfield shift relative to the neat peptide.

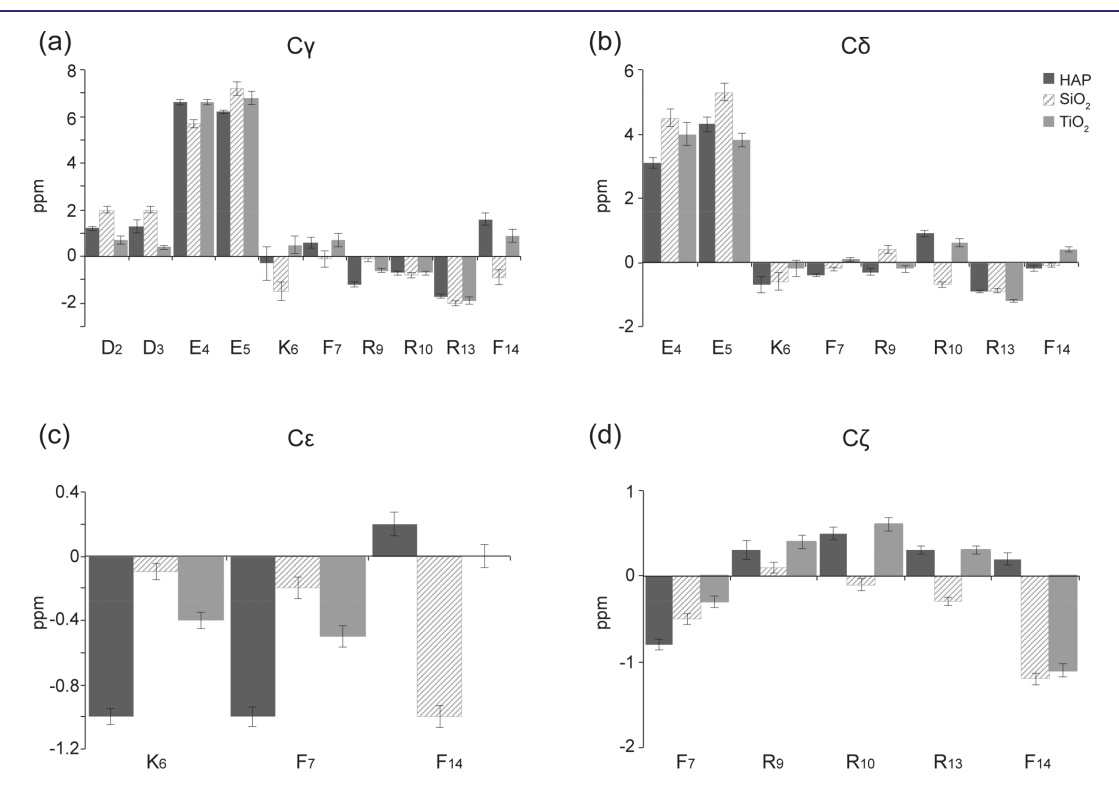


Figure 6. Side-chain Δ CS plots showing chemical shift perturbations for (a) 13 C γ shifts, (b) 13 C δ shifts, (c) 13 C ϵ shifts, and (d) 13 C ζ Δ CS. Δ CS for SNa15 on HAP (black), SiO₂ (hatched), and TiO₂ (gray) are in reference to neat SNa15. Positive changes indicate a downfield shift while negative changes indicate an upfield shift relative to the neat peptide.

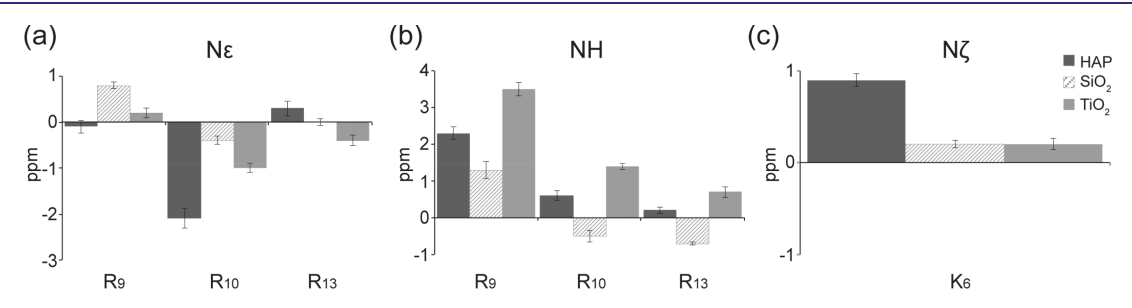


Figure 7. Side-chain Δ CS plots showing chemical shift perturbations for (a) 15 N ε , (b) 15 NH, and (c) 15 N ζ . Δ CS for SNa15 on HAP (black), SiO₂ (hatched), and TiO₂ (gray) are in reference to neat SNa15. Positive changes indicate a downfield shift while negative changes indicate an upfield shift relative to the neat peptide.

SNa15 that are unique to each mineral phase and might be useful in highlighting the unique conformation of SNa15 adsorbed to each mineral phase, which we further explore with MD simulations.

 Δ CS values for the side-chains of SNa15 at different surfaces are plotted in Figure 6. SNa15 experiences downfield shifts for

the 13 C γ of D2 and D3 and the 13 C δ of E4 and E5 across all mineral surfaces. These spins correspond to the side-chain carboxyl groups in the aspartic acid and glutamic acid residues in the N-terminus of SNa15, respectively. The 13 CO shifts of E4 and E5 are also accompanied by large downfield shifts of the 13 C γ spins for SNa15 upon adsorption to all three mineral

surfaces. The basic residues of SNa15 (K6, R9, R10, and R13) generally experience less pronounced and less consistent perturbations across the three surfaces. There is a consistent upfield shift for both the 13 C γ and 13 C δ spins of R13 in SNa15. Additionally, there is an upfield shift of the ${}^{13}\text{C}\varepsilon$ spin of K6 upon adsorption to HAP and TiO2, although not SiO2. Typically, upfield shifts of lysine ${}^{13}\text{C}\varepsilon$ spins indicate proximity to a negatively charged mineral surface.⁵⁸

Figure 7 shows the ^{15}N side-chain ΔCS values for different surfaces. Downfield perturbations are observed for R9 15N shifts upon adsorption to HAP (2.3 ppm), SiO₂ (1.3 ppm), and TiO₂ (3.5 ppm), indicating interactions with the phosphate buffer and/or the surfaces. The K6 $^{15}N\zeta$ spin also experiences a downfield perturbation, albeit less pronounced, upon adsorption to HAP (0.9 ppm), SiO₂ (0.2 ppm), and TiO_2 (0.2 ppm).

SNa15 Secondary Structure Predictions from TALOS-**N.** Following the conventional practice for structure prediction from ssNMR data, the backbone ¹³C chemical shifts for SNa15 were input to the TALOS-N 59 program, that predicts the ϕ/ψ torsion angles (Supporting Information). Chimera⁶⁰ was used to visualize the structure that corresponds to these predicted torsional angles (Figure 8 and Figure 9). Figure 8 shows that

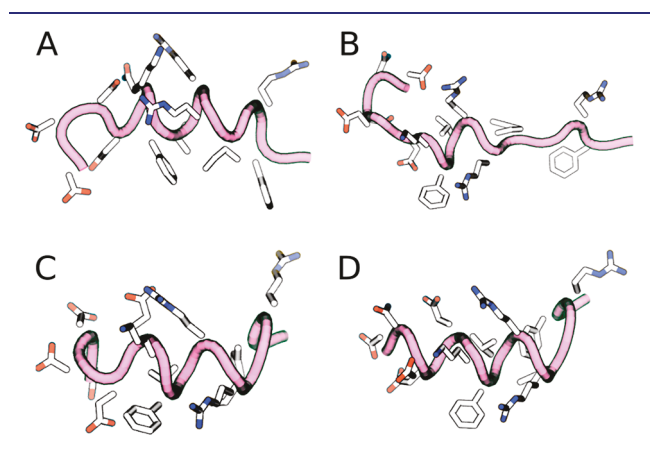


Figure 8. Chimera 60-generated models of (a) SNa15-neat, (b) SNa15-SiO₂, (c) SNA15-HAP, and (d) SNa15-TiO₂ using TALOS-N⁵⁹-predicted torsion angles from experimentally obtained chemical shifts. Each peptide is shown from N-terminus to C-terminus right-toleft.

SNa15 has some α -helical structure in each surface-bound state and that SNa15 is largely unstructured when adsorbed to SiO₂. For neat SNa15, the ϕ/ψ torsion angles for E4-I11 are clustered around the accepted α -helical values (-57/-47), while the ϕ/ψ torsion angles for R13 and F14 are clustered around (-80/+150), indicating a loss of helicity at the Cterminus and a more extended secondary structure. Largely, the torsion angles upon adsorption to HAP are similar to those in the neat state, as evident by the similarity in structures of A and C (Figure 8). In the case of HAP, residues E5-I11 exhibit α -helical character, while residues in the N-terminus (D2-E4), and C-terminus (R13-F14) exhibit more extended structures. In contrast, upon adsorption on TiO_2 , the α -helix is extended farther into the N-terminus; the ϕ/ψ angles for D2-I11 are all clustered around α -helical values, although the C-terminus remains extended, as seen in HAP. Remarkably, the structure of SNa15 differs greatly upon adsorption to SiO₂ when

compared to the other systems. The helical region of SNa15-SiO₂ is limited to K6-R9.

The end-view of each predicted structure is visualized in Figure 9 to highlight helical content and the relative orientation of the side-chains. In the mineral systems, F7 and F14 are pointing in different directions. This is consistent with chemical shift data, relaxation dynamics $(T_1/T_{1\rho})$, 21,28 13 C- $\{^{31}$ P} REDOR, 21 2 H ssNMR, 28 and NEXAFS 25 data, which all conclude that F7 is far from the HAP surface (at least 7 Å) while F14 is close to (within 4 Å) and interacting with the surface. The Δ CS values in this study support this theory, because there are significant perturbations for F14 (13 C γ , 13 C δ , $^{13}C\varepsilon$, and $^{13}C\zeta$ data), yet much smaller perturbations for the same shifts of F7. Further, it has been posited that F14 is in a near-parallel orientation to HAP, thus exposing the delocalized electrons in the phenyl ring.61

SNa15 Secondary Structure Predictions of Adsorbed Peptides from MD Simulations. MD is used to generate an ensemble of conformations of the peptide consistent with the experimentally measured chemical shifts. The backbone ¹³CO, $^{13}C\alpha$, and $^{13}C\beta$ chemical shift data for SNa15-HAP, SNa15-SiO2, and SNa15-TiO2 were used to restrain an ensemble of configurations using the metadynamic metainference approach⁵¹ (see Methods). The restraints are applied to the average chemical shifts across many simulation replicas, thereby limiting the average deviation of the backbone chemical shift to be within the error predicted by experiments. The calculated side-chain chemical shifts are not directly used in the simulations or analysis of the clusters and provide a posteriori validation of our approach. Root mean squared errors (RMSE) of the backbone (training error) and side chain (validation error) for the surface adsorbed peptides are provided in Table 2. We see that the error in both the backbone and side chain chemical shifts are between 1.48 and 2.25 ppm, which denotes agreement with experimental data (experimental error ~2 ppm), providing strong evidence that the ensemble of peptide conformations generated by the metadynamic metainference simulation are consistent with the experimental data.

We next determined the most likely conformations of the peptide generated by the MD simulation by performing a clustering (see Methods). The center of the top three most likely clusters of peptide backbone conformations (and their weights determined from postprocessing of the metadynamics simulations) along with the representative structure from TALOS-N are shown in Figure 10. For the case of SiO₂, all conformations are random coils with a helical middle section. Noticeably, the structure predicted by TALOS-N has the same structural motif. The MD-predicted structures of SNa15 on HAP show similar amounts of secondary structure, with more variance in the number of helical turns in the center. For both ${\rm TiO_2}$ and HAP surfaces, the structure predicted by TALOS-N displays a greater level of helicity (with unstructured ends) than the MD-predicted structure. However, the top three peptide structures encompass the helical components present in the TALOS-N structures. This demonstrates the need to view the structure of SNa15 on mineral oxide surfaces as an "ensemble" and not a single entity. We note that in all cases, the exact structure predicted by TALOS-N can be found within the biased MD simulations, although it does not appear in the top three reweighted cluster centers shown here.

To ascertain which residues are interacting with the surface, the top three clusters were placed near the respective surface

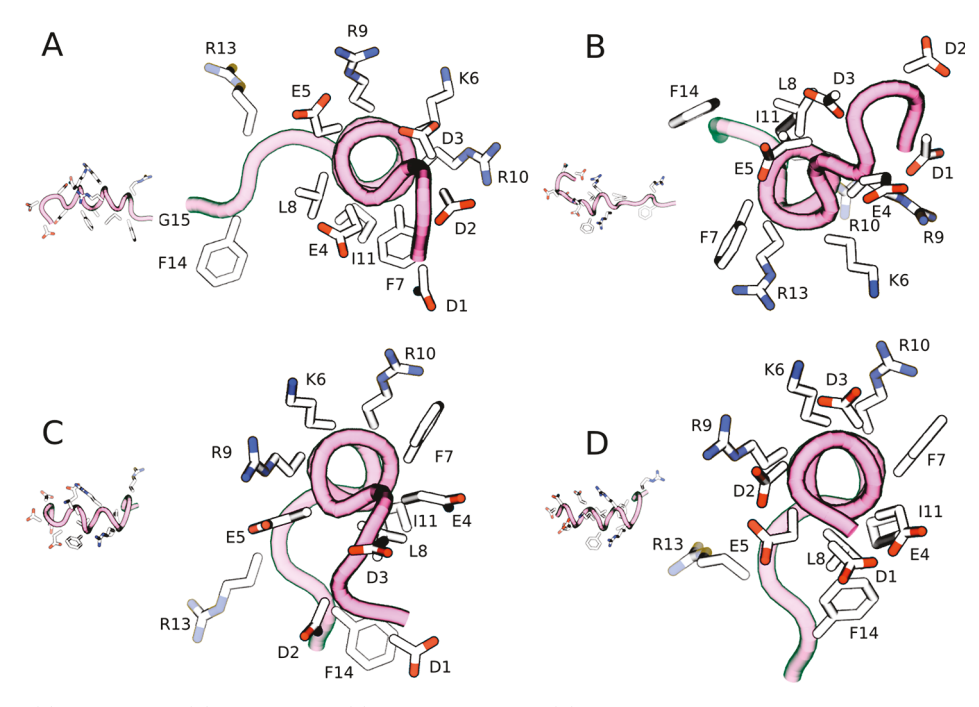


Figure 9. End-view of (a) SNa15-neat, (b) SNa15-SiO₂, (c) SNA15-HAP, and (d) SNa15-TiO₂ with each residue labeled. Structures are visualized with Chimera 60 using torsion angles predicted by TALOS-N. 59

Table 2. Root-Mean Squared Error of the Backbone and Side-Chain

| simulation | RMSE of backbone | RMSE of side-chains |
|------------------------|------------------|---------------------|
| SNa15-HAP | 2.17 | 1.59 |
| SNa15-SiO ₂ | 2.25 | 1.75 |
| SNa15-TiO ₂ | 1.91 | 1.48 |

and simulated for 50 ns (with the backbone restrained using an RMSD restraint on the $C\alpha$ atoms) (see Figures S4–7). For the case of the HAP surface (Figure S4), SNa15 is anchored to the interface by a mixture of basic (R9, K6, and R10) and acidic

(D1, D2, and E5) residues. Because the surface is neutral overall, and has local pockets of positive and negative charge, it is understandable that the peptide needs both types of binding residues to bind to the surface. The TiO₂ surface is a negatively charged surface. Consequently, basic residues (R10, and K6) allow SNa15 to bind to the surface (Figure S5). Acidic residues (D1, D2, and D3) interact with mobile sodium ions. Similar to the TiO₂ surface, the SiO₂ surface is also negatively charged and neutralized with mobile, displaceable sodium ions. Therefore, SNa15 is also anchored with basic residues only (R13 and R9) (Figure S6). Notably, neutral, hydrophobic

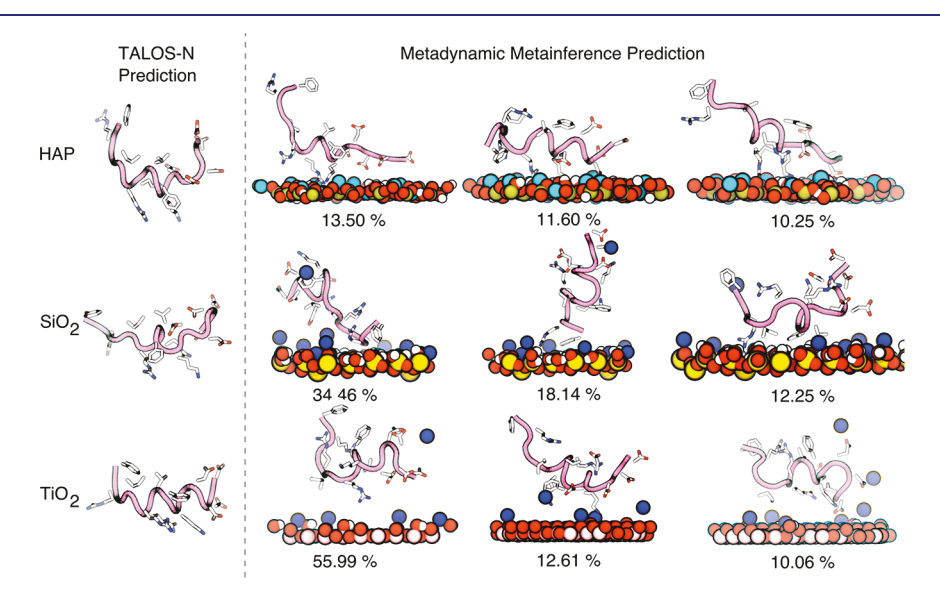


Figure 10. TALOS-N prediction and metadynamics metainference predictions of the structures of SNa15 on HAP (top), SiO₂ (center), and TiO₂ (bottom) surfaces. The peptide backbone is shown in mauve with tube structure. Surface atoms are colored blue for sodium ions, light blue for calcium, red for oxygen, yellow for silicon. The heavy side-chain atoms on the protein are rendered with licorice and colored blue for nitrogen, red for oxygen, and white for carbon. The percentages of the MD configurations refer to the weight of that cluster within the structural ensemble.

residues like F14, F7, and I11 also approach the surface. On approach, F14 and F7 lay flat on the surface.

Additionally, the contact profile of individual residues with the surface is explored. Several residues show a bimodal distribution of contacts on the SiO₂ surface (D2, D3, K6, F7, R9, and F14) (Figure S7). Most N-terminus residues of SNa15 are closer to the surface on SiO₂ and TiO₂ than they are on the HAP surface (Figure S7). Notably, all SNa15 residues are in closer contact with the SiO₂ surface than the other surfaces. We hypothesize that greater contact with the surface might promote the SNa15 residues to unfold more, thus SNa15 has much less helical content on the SiO₂ surface.

Finally, the distribution of secondary structure elements along the peptide is determined (Figure S8). The results indicate helical structures in the middle residues of SNa15 peptide on all three mineral surfaces. However, the peptide is more likely to be helical on the ${\rm TiO_2}$ surface, as also seen in the TALOS-N predictions. SNa15 has significant random coil structure on the HAP surface. Finally, SNa15 shows distinct bends on the ${\rm SiO_2}$ surface, which is also evident in the TALOS-N prediction.

DISCUSSION

Both the structure of the protein and the interaction of its sidechains with the surface are integral to the process of recognition of biomineral surfaces by proteins. Expectedly, the foundational goals in this field are centered around the determination of protein secondary structure, the evaluation of changes in structure upon adsorption, and the estimation of the proximity or orientation of amino acids to the surface. To further these goals, we have chosen the model peptide SNa15 and elucidated its structure upon binding to three naturally occurring mineral surfaces (HAP, SiO₂, and TiO₂). In fact, we have demonstrated an integrated approach that pairs experimental data with MD simulations to make more robust predictions about the ensemble of surface adsorbed structures. Experimentally, we used 1D and 2D ssNMR techniques to determine the secondary structure of SNa15 in the neat, i.e. unadsorbed solid state, and when adsorbed to HAP, SiO₂, and TiO₂ surfaces. On the modeling front, we used the structure prediction software TALOS-N, and classical all-atom MD simulations (with metadynamic metainference enhanced sampling) to generate an ensemble of conformations of the peptide on the surface, which are consistent with the experimental data.

Overall, the backbone (13 CO, 13 C α , and 13 C β) chemical shift data and subsequent TALOS-N 59 predictions indicate that SNa15 is helical (with unraveling at the termini) when neat and when adsorbed to HAP and TiO₂. In contrast, the peptide is predicted to be largely unfolded on the SiO₂ surface. The picture, when viewed from the perspective of integrated MD+ssNMR is more nuanced, with a need to explore in more detail the full conformational ensemble.

Further, we explore the interaction of various amino-acid side-chains with the surface via the Δ CS for the side-chain 13 C spins. Notably, large downfield perturbations in the Δ CS of E4, E5, and F14 (in all cases) suggest that they are interacting with each surface. There are large downfield perturbations for the side-chain 13 C γ and 13 C δ spins of E4 and E5 (Figure 6a,b). In fact, this CS perturbation is attributed to the decreased shielding of the carboxyl group due to its interaction with the surface. See Fernandez et al. See also noted similar downfield shifts in 13 C δ spins (\sim 2 ppm) in their study of poly-L-glutamic acid

adsorbed on HAP and SiO₂. In our study, these downfield shifts range from 3 to 5.3 ppm indicating a stronger effect than that seen by Fernandez et al. Moreover, because the perturbations are roughly the same magnitude within error for both residues, this suggests a similar degree of contact with the surface. This contrasts with the predicted behavior of SN15 and statherin on HAP, where only E5 was proposed to interact with HAP. In fact, MD simulations predict that E4 and E5 have a much higher degree of conformational flexibility (Figure S7) on HAP compared to SiO₂ and TiO₂. Notably, NMR-derived side-chain constraints were not included in the MD simulation, therefore some deviations in the side-chain behavior is expected.

Among the aromatic groups, we observe that F14 is also interacting significantly with the surface. The role of phenylalanine residues in the binding of statherin to HAP has been studied extensively. 21,25,28 Gibson and co-workers 21 studied the role of F7 and F14 in SN15 adsorption to HAP through isotropic chemical shift perturbations, ¹³C{³¹P} REDOR, and T₁₀ relaxation measurements. They found that when compared to F7, F14 is closer to the surface and is more dynamically constrained. In fact, F7 is observed to be oriented away from the HAP surface.²¹ The study by Weidner and coworkers²⁵ used NEXAFS and SFG also corroborates this observation. Correspondingly, in this study, we note large Δ CS for F14 and minimal Δ CS for F7 (Figures 5 and 6). MD simulations also predict the interaction of F14 with SiO₂. In fact, the ^{13}CO and $^{13}\text{C}\alpha$ chemical shift data also show that F14 behaves differently in HAP than the other two surfaces.

In the case of basic residues, there are negligible perturbations for most of the side-chain ¹³C spins for K6, R9, and R10. MD simulations also show that other basic residues (K6, R9, and R10) are away from the surface (Figure S7). This suggests that these residues do not specifically adsorb to or identify any of these surfaces. In fact, previous studies where the 4 basic residues (K6, R9, R10, R13) of statherin were mutated to alanine have shown that individually, none of these residues are crucial to binding. However, as a group they act to decrease the overall charge of statherin, thus reducing repulsive protein—protein interactions and promoting a higher surface affinity and coverage. ³⁰

In contrast, the R13 13 C γ and 13 C δ spins experience significant perturbations in the range of -0.9 to -2 ppm. This suggests that R13 interacts with the surfaces while the remaining basic residues do not. From the end-view of TALOS-N predicted structures (Figure 9), it is evident that the R13 side-chain is oriented on the same face of SNa15 as E4, E5, and F14 (the residues that are hypothesized to interact with the surfaces). The behavior of R13 is corroborated with MD simulations only in the case SiO₂.

Finally, we observe that D2 and D3 are also crucial to the recognition of surfaces. In the case of HAP, D2 and D3 are oriented along the hypothesized binding face of SNa15. These residues experience a downfield shift of 1.2 and 1.3 ppm, respectively, upon adsorption. This is also true for adsorption on SiO_2 , because D2 and D3 both experience a downfield shift of 2 ppm. However, in the case of TiO_2 , only D2 is oriented along the binding face (predicted by a significant ΔCS in D2 only). From MD simulations, we see that D2 contributes to the binding of SNa15 to all surfaces (Figure S7) while D3 contributes to the binding to SiO_2 and TiO_2 .

On the basis of the information above, we hypothesize that the binding domain of SNa15 consists of some residues from N-terminus (D2-E5) and C-terminus (R13 and F14) for binding to HAP and SiO₂. For the case of TiO₂, D3-E5, R13, and F14 residues contribute to binding. MD simulations predict that SNa15 binds from the N-terminus on the HAP and TiO₂ surfaces, and from the C-terminus on the SiO₂. The residues composing the hypothesized binding domain are all oriented on the same face of SNa15 and all experience significant chemical shift perturbations upon adsorption. In fact, the lack of α -helical character in the N-terminus allows consecutive acidic residues to be positioned along the same face and interact completely with the surface.

Because SNa15 is comparable to other model peptides (SN15) and its parent protein statherin, it is possible to compare the behavior of SNa15 with previously reported observations about the other peptides. In fact, prior studies of statherin and SN15 on HAP were based on distance measurements obtained from dipolar couplings between ¹³C and ¹⁵N spins within the peptides and between ¹³C spins in peptide side chains and ³¹P spins in the HAP surface. Because these studies and the current studies result in predictions of the peptide structure, it is useful to compare these results, albeit qualitatively. For example, the distorted helical structure obtained for SNa15 on HAP, obtained by analysis of the 13 CO, 13 C α , and 13 C β chemical shifts via TALOS and MD simulations, is in agreement with earlier dipolar coupling-based studies of the structure of SN15 and statherin on HAP. 15,31,37 Our present study of SNa15 and prior studies of statherin and SN15 find that the acidic N-termini of SNa15 and SN15 interact strongly with the HAP surface, but details of exactly which side chains are involved in surface interactions differ. Downfield changes to the chemical shifts of the γ and δ carboxyl ¹³C spins in SNa15's D2D3E4E5 moiety observed upon adsorption to HAP indicate interactions with the HAP surface. Relaxation and chemical shift line shape studies of pS2 and pS3 in SN15 on HAP similarly find that these N-terminal amino acids are anchored to the surface, 36 but a $^{13}\text{C}\{^{31}\text{P}\}$ REDOR study finds that the ${}^{13}{\rm C}\delta$ spin of E5 is much closer to the HAP surface than the carboxyl group of E4.¹⁹ Based on ¹³Cζ upfield chemical shift changes upon adsorption to HAP, only R13 is assumed to interact with the HAP surface in SNa15, while a ¹³C{³¹P} REDOR study of statherin on HAP finds that the 13 C ε spin of K6 and 13 C ζ spins of R9 and R10 are close to the HAP surface. Some of these differences may result from variations in local secondary structure, where for example the substitution of D for pS at positions 2 and 3 in SNa15 may perturb the local helical structure making it possible to simultaneously expose E4 and E5 in SNa15 to the surface. The apparent differences between exposure of basic amino acids in SN15 and SNa15 to the HAP surface may similarly result from structural changes in the acidic portion of the N-terminus that perturb the surface orientation of the basic amino acids.

Another factor to consider is the effect that the orientation of the side chain has on Δ CS values. In a study of SK rich peptides in SiO₂ and TiO₂ composites, density functional theory (DFT) calculations showed that the chemical shift of $^{13}\text{C}\varepsilon$ spins in lysine side chains has a large upfield ΔCS when the side chain is oriented perpendicular to the surface, but the ΔCS is greatly diminished for $^{13}C\varepsilon$ when the side chain is oriented parallel to the surface. 62 Also, for lysine $^{13}C\varepsilon$ spins Δ CS values drop off rapidly as a function of the distance between the amine group and the surface. For example, when the distance from the lysine side chain amine to the SiO₂

surface exceeds 3 Å Δ CS perturbations are comparable to experimental error.

Some of the results obtained in our study of SNa15 mineral interactions are similar to results reported in other studies of statherin-mineral interactions. For example structural dispersion of SN15 on HAP was observed in a solid-state NMR study by Chen et al.⁶³ Those workers observed two sets of cross peaks for K6 in the 1D ¹³C-¹³C correlated spectrum. The 13 C α chemical shift of the major component (66%) was close to that observed for free (i.e., helically structured) SN15 while the minor component chemical shift was close to random coil. A study of differential adsorption of statherin and the statherin peptide SN21 on HAP and silica by ellipsometry⁶⁴ showed higher adsorption levels for both peptides on HAP versus hydrophilic silica. This observation was attributed by the authors in part to repulsion between the negatively charged surface and the negatively charged side chains at the N-terminus.

However, a significant result of our study is that differential adsorption of SNa15 on TiO2 and HAP versus SiO2 is accompanied by differential structuring on these surfaces, i.e., more helical structuring on TiO2 and HAP versus SiO2. If this differential structuring effect can be demonstrated for other proteins on mineral surfaces, then the detailed surface structure of the protein and the arraying of side chains is an important component of its surface interactions and may, for example, explain in part the affinity of tissue cells for particular implant coatings. It has long been known that interactions between tissue-generating cells and implant surfaces are mediated by a proteinaceous layer. 65-67 Ideally, a layer of specifically adsorbed proteins promotes cell adhesion to the implant surface and normal cellular response, leading ultimately to integration of the implant with the surrounding tissue. Nonspecific adsorption of proteins or the presence of proteins in an unstructured or otherwise unrecognized state may result in a foreign body response and implant failure. For example, it has been observed that osteoblasts differentiation is enhanced on TiO₂ coatings versus SiO₂ coating.⁶⁸ Although further studies of protein surface structures are required to support a general explanation, the ability of TiO2 to support a layer of structured adhesion proteins may contribute to its ability to support osteoblast differentiation.

CONCLUSION

This study of the adsorption of SNa15 onto HAP, SiO2, and TiO₂ surfaces demonstrates an integrated approach that pairs ssNMR with advanced MD simulations as a means to predict ensembles of surface-bound peptide structures. Measured adsorption isotherms and companion structure predictions from the software TALOS-N provide additional characterization of the systems. In contrast to using TALOS-N to predict a single set of dihedral angles, the integrated approach allows for structure prediction of an entire conformational ensemble with average backbone chemical shifts constrained to the measured experimental values. This approach is thus a promising way to estimate not only the conformational ensemble but also the key binding residues to the surface and orientation of the adsorbed biomolecule.

Although this method can be applied to many peptide/ surface systems in the future to study biomineralization processes, the approach has potential areas for future investigation. First, there is a continued need to improve surface potentials and representation of accurate surface chemistries for use in MD simulations of peptide adsorption, even with metadynamic metainference approach to help overcome systematic errors. Second, DFT can be used to further assess the accuracy of our approach by providing estimates of the surface response of individual (or small groups) amino acids in relationship to the orientation of the molecule and distance to the surface. DFT remains far too computationally expensive to use in the same manner as we have in this work (i.e., structure prediction), but holds great promise to study the accuracy of the SHIFTX and CAM-SHIFT methods for peptides on surfaces.

METHODS

Peptide Synthesis. All natural and uniformly labeled ¹³C and ¹⁵N amino acids were purchased from either Sigma-Aldrich (St. Louis, MO) or Cambridge Isotope Laboratories (Tewksbury, MA). Preloaded Fmoc-protected Wang resin was purchased from EMD Millipore (Billerica, MA). All other reagents were purchased from Sigma-Aldrich (St. Louis, MO) and used without purification. Peptides were synthesized on a CEM Liberty Blue peptide synthesizer using a standard 9-fluorenylmethoxycarbonyl (FMOC) and tert-butyl protection scheme. Preloaded Fmoc-protected Wang resin was used for solid phase synthesis. Peptides were cleaved from the resin in a 10 mL solution of 95:2.5:2.5 trifluoroacetic acid:triisopropylsilane (TIPS):water mixture per 1.0 g of peptide/resin. The resulting filtrate was added dropwise into cold tert-butyl methyl ether, followed by centrifugation and three rinses of the resulting solids with 40 mL of cold tert-butyl methyl ether. Peptides were purified using RP-HPLC (Varian ProStar HPLC, Alltima WP C4 column, 5 mL/min, eluent A: water with 0.2% TFA, eluent B: acetonitrile with 0.2% TFA), using a gradient of 15-50% B over 40 min. Chromatograms were generated by observing the UV absorbance at 254 nm, and the analyte was verified by mass spectrometry. The fractions were then lyophilized, resulting in the pure peptide.

Surface Area Determination. HAP (product number 677418; a synthetic, crystalline nanopowder with a reported particle size <200 nm), SiO₂ (product number 637246; a spherical, porous nanopowder with a reported particle size of 5-20 nm), and TiO₂ (product number 637262; a rutile titanium(IV) oxide nanopowder with a reported particle size <100 nm) nanoparticles were purchased from Sigma-Aldrich (St. Louis, MO) and used without purification. The surface area of the HAP, SiO2, and TiO2 nanoparticles was determined using a Nova 4200e Surface Area and Pore Size Analyzer from Quantachrome Instruments. BET measurements showed a surface area of 34.4 m²/g for HAP, 331.9 m²/g for SiO₂, and 28.6 m²/g for TiO₂ nanoparticles.

Adsorption Isotherms. Known concentrations of SNa15 (1 mL) were equilibrated with 10 mg of HAP, SiO2, or TiO2 nanoparticles for 4 h in phosphate buffer (100 mM, pH = 7.4). After adsorption, the solid nanoparticles were separated from the mixture via centrifugation at 13000g for 15 min. The peptide concentrations in the supernatant solutions were measured using an Agilent 8453 Diode Array UV-vis Spectrophotometer and compared with the initial concentrations.

ssNMR Sample Preparation. SNa15 (2 mM, 5 mL) was equilibrated with 60 mg of mineral nanoparticle for 4 h in phosphate buffer (100 mM, pH = 7.4). After adsorption, the solid was separated from the mixture via centrifugation at 13000g for 15 min. The supernatant was discarded, and the remaining solid was dried in vacuo.

ssNMR. All solid-state NMR experiments were conducted using a 16.4 T magnetic field (proton resonant field of 700.18 MHz) on a Bruker Avance III spectrometer fitted with a ¹H {¹³C, ¹⁵N} 3.2 mm MAS probe. The spinning speed for all experiments is 15 kHz \pm 5 Hz, and is regulated by a Bruker MAS controller unit. All experiments were run at room temperature. 1D ¹³C CP MAS experiments were collected using a 4 μ s proton $\pi/2$ pulse, a contact time of 1.2 ms, and a recycle delay of 2 s. Neat samples required 2k scans while adsorbed samples required 8k scans. 1D 15N CP MAS experiments were collected using a 4 μ s proton $\pi/2$ pulse, a contact time of 2 ms, and a

recycle delay of 2 s. Neat samples required 4k scans while adsorbed samples required 32 k scans. All ¹³C chemical shifts reported were indirectly referenced to tetramethylsilane (TMS) in the solid-state using adamantane (δ = 38.48 ppm).⁶⁹ All ¹⁵N chemical shifts reported were indirectly referenced to NH_3^+ in the solid-state using glycine (δ = 33.4 ppm). 70 2D 13 C $^{-13}$ C DARR experiments were collected with a 1.2 ms contact time, a 4 μ s proton $\pi/2$ pulse, and a 4 μ s 13 C $\pi/2$ pulse. Mixing times were 60 ms. For neat samples, there were 256 points in the indirectly detected dimension (F1) and 1k points in the directly detected dimension (F2). For adsorbed samples, there were 128 points in F1 and 1k points in F2. Again, the chemical shifts reported were indirectly referenced to TMS in the solid-state using adamantane ($\delta = 38.48 \text{ ppm}$).

Molecular Dynamics Simulations. System Setup. The structure of SNa15 peptide when adsorbed onto HAP, SiO₂, and TiO₂ surfaces was probed using classical all-atom molecular dynamics simulations. The peptide was modeled using the AMBER99SB-ILDN force field.⁷¹ Water was modeled using the SPC/E water model.⁷² HAP and SiO₂ were modeled using the INTERFACE force field, ⁷³ while the TiO₂ was modeled using the force field by Predota et al.⁷⁴ (details about surface construction in SI). These models were chosen according to previously published studies of peptide and surfaces.^{75–79} The HAP surface was neutral, whereas the negatively charged TiO₂ and SiO₂ surfaces were neutralized by 72 and 80 Na+ ions, respectively. The peptide had a net negative charge of -1 which was neutralized by a single Na⁺ ion.

For each peptide-surface system, a slab of the inorganic surface was created, and the peptide was placed near the surface. This system was then solvated with water (7935 waters for HAP, 8273 waters for SiO₂, and 8134 waters for TiO₂). Unfavorable contacts during this packing were removed by using a steepest descent algorithm that minimized the energy of the system. The pressure of the system was equilibrated to 1 bar by propagating the system in the NPT ensemble (temperature = 300 K; pressure = 1 bar) for 1 ns. The semi-isotropic version of Berendsen barostat⁸⁰ ($\tau = 1.0 \text{ ps}$) was used so that only the z-axis of the box changed to correct the pressure of the system. The Bussi-Donadio-Parrinello thermostat⁸¹ ($\tau = 0.1$ ps) was used to maintain the temperature at 300 K. For the production run, the system was propagated in the NVT ensemble (300 K) for a total of 2 μs with 4 replicas (500 ns/replica). For all simulations, long-range electrostatics were treated with particle-mesh Ewald summation.⁸² A cutoff of 1.0 nm was used for Lennard-jones and Coulombic interactions. All bonds between hydrogens and heavy atoms were constrained using the LINCS algorithm⁸³ allowing for a simulation time step of 2 fs. All simulations were conducted using GROMACS 2016.

Biasing Scheme. We used the parallel bias metadynamics⁸⁵ scheme, which allows for efficient sampling of such high-dimensional free energy landscapes. To ensure that all binding conformations of the peptide were explored, we biased 4 collective variable -3 for structural elements of the peptide (radius of gyration, α -helical and 3₁₀-helix coordination numbers) and 1 for the distance of the peptide from the surface. The radius of gyration was calculated using all α carbon atoms. Coordination numbers were calculated using carbonyl oxygen and amide hydrogen contacts within 0.30 nm of the i^{th} and $i + i^{th}$ 4th residues for the α helix and i^{th} and i + 3th residues for the 3_{10} helix. The distance was calculated by using the z-distance between the center of mass of all α -carbon atoms and a reference surface atom. The peptide was restrained to explore only distances below 2 nm so that the peptide only explores surface-bound structures. The parameters for the bias were: initial hill height of 1.2552 kJ/mol, hill deposition pace of 1 hill/500 steps, biasfactor of 10, and temperature 300 K. The collective variables had hill widths of 0.5 nm (radius of gyration and distance), and 0.1 (α -helical and 3₁₀-helix coordination numbers).

The combination of classical MD with an enhanced sampling scheme promotes the exploration of multiple conformation states of the peptide. However, the prevalence of specific conformations can be overpredicted or under-predicted according to the accuracy of the force field used. 86 To correct for these inaccuracies and ensure that

experimentally relevant conformations are correctly represented in the simulation, we combined the parallel bias enhanced sampling method with metainference. 51,52 Using Bayesian inference, this approach allows for the NMR chemical shifts to be used as restraints on the predicted chemical shifts averaged over an ensemble of peptide conformations. Chemical shifts were calculated on-the-fly using CAMSHIFT⁵⁰ (as implemented in the PLUMED 2.4⁸⁷ library). Our criteria for assessing convergence, and demonstration of convergence of the calculations are discussed in the SI (Figures S8-10).

Validation of Peptide Structures. After the production simulations are completed, the simulation trajectories are analyzed to find the most representative structures of the surface-bound peptide. Because the trajectories are large, every 50th frame is used for analysis, resulting in 20 000 frames. Further, some frames were excluded from the trajectory as mentioned in Section 1 in the SI. Finally, the chemical shifts calculated at every frame. Backbone chemical shifts were calculated on the fly using CAMSHIFT⁵⁰ as implemented in PLUMED, whereas side-chain chemical shifts were calculated using SHIFTX⁴⁹ because CAMSHIFT does not provide side chain chemical

At the end of the simulation, we can use the accumulated bias potential as weights to calculate the free energy with respect to another variable (separate from the variables biased in the original simulation).⁸⁸ A weight (= $e^{V/kT}$, where kT = 2.5 kJ/mol at 300 K, Vis the bias at each frame) is assigned to each frame using the bias potential as a quasi-static bias potential. These weights were used to calculate the weighted average chemical shift from the trajectory, following the protocol of Torrie and Valleau. 89 The root-meansquared error of the backbone and side-chain chemical shifts, with reference to the experimentally determined values, were calculated using the formula:

RMSE =
$$\left(\sum_{i=1}^{N} (CS_{i,predicted} - CS_{i,exp})^{2}\right)^{0.5}$$

Detection of Top-Weighted Peptide Conformations. The structures of the peptide in the trajectory are identified and clustered using the gromos 90 method (RMSD calculation using α -carbon atoms with cutoff of 0.20 nm). Then, the cluster number assigned to each frame of the trajectory is reweighted with the above-mentioned weights.

Detection of Top-Weighted Peptide Orientations. To study relaxation of the side chains and orientation of the peptides on the surfaces, the top three weighted conformations for each surface were extracted and simulated for 50 ns in the NVT ensemble (300 K). The backbone was held rigid during the simulation using a restraint on the RMSD of the α -C carbons using a harmonic restraining potential (value = 0.15 nm; κ = 10 000.0). No other bias was added during these simulations. The trajectories were viewed in VMD to identify the residues that interact with each surface (shown in Figures S4-6). For a quantitative analysis of contacting residues, the normal surface distance of side-chain atoms (C γ , C δ , C ε , and C ζ) from a reference surface atom was calculated for the whole trajectory. The probability of the occurrence of the side-chain atom at a certain distance from the surface was calculated using the kernel density estimation technique (shown in Figure S7)

Detection of the Secondary Structure of Each Residue. A secondary structure was assigned to each residue of SNa15 in each frame of the trajectory using the do_dssp functionality of the GROMACS simulation engine. The probability of each residue being in a certain secondary structure was calculated using the reweighting procedure mentioned above.

ASSOCIATED CONTENT

S Supporting Information

The Supporting Information is available free of charge on the ACS Publications website at DOI: 10.1021/jacs.8b10990.

Additional 2D 13C-13C DARR for all systems studied and associated chemical shift assignments for side chains and backbones, backbone dihedral angles generated from TALOS-N for all systems, top binding poses for bound peptides for three surfaces determined from MD and associated analysis of side chain binding propensity and secondary structure, additional simulation details including convergence of bias potentials, surface parameters and analysis procedures(PDF)

AUTHOR INFORMATION

Corresponding Authors

*drobny@chem.washington.edu *jpfaendt@uw.edu

ORCID ®

Jim Pfaendtner: 0000-0001-6727-2957 Gary P. Drobny: 0000-0002-7293-1897

Author Contributions

⁺Authors contributed equally to this work.

Notes

The authors declare no competing financial interest.

ACKNOWLEDGMENTS

G.P.D. acknowledges National Institutes of Health Grant RO1-GM109417. G.P.D. and J.P. acknowledge grant NIH R21 A126113 and National Science Foundation Grant MCB-1715123. This work was facilitated using computational, storage, and networking infrastructure provided by the Hyak supercomputer system, supported in part by the University of Washington and the UW Student Technology Fee Proposal program and NSF MRI program CHE-1624430. G.P.D. also acknowledges support from subcontract ANSK-0119-16 and helpful conversations with Professors Havard J. Haugen and S. Petter Lyngstadaas of the Department of Biomaterials, Institute for Clinical Chemistry University of Oslo.

REFERENCES

- (1) Elhadj, S.; De Yoreo, J. J.; Hoyer, J. R.; Dove, P. M. Role of Molecular Charge and Hydrophilicity in Regulating the Kinetics of Crystal Growth. Proc. Natl. Acad. Sci. U. S. A. 2006, 103 (51), 19237-19242.
- (2) Boskey, A. L.; Maresca, M.; Ullrich, W.; Doty, S. B.; Butler, W. T.; Prince, C. W. Osteopontin-Hydroxyapatite Interactions in Vitro: Inhibition of Hydroxyapatite Formation and Growth in a Gelatin-Gel. Bone Miner. 1993, 22 (2), 147-159.
- (3) Shiraga, H.; Min, W.; VanDusen, W. J.; Clayman, M. D.; Miner, D.; Terrell, C. H.; Sherbotie, J. R.; Foreman, J. W.; Przysiecki, C.; Neilson, E. G. Inhibition of Calcium Oxalate Crystal Growth in Vitro by Uropontin: Another Member of the Aspartic Acid-Rich Protein Superfamily. Proc. Natl. Acad. Sci. U. S. A. 1992, 89 (1), 426-430.
- (4) Naka, K.; Chujo, Y. Control of Crystal Nucleation and Growth of Calcium Carbonate by Synthetic Substrates. Chem. Mater. 2001, 13, 3245-3259.
- (5) Söllner, C.; Burghammer, M.; Busch-Nentwich, E.; Berger, J.; Schwarz, H.; Riekel, C.; Nicolson, T. Control of Crystal Size and Lattice Formation by Starmaker in Otolith Biomineratization. Science (Washington, DC, U. S.) 2003, 302 (5643), 282-286.
- (6) Kröger, N.; Poulsen, N. Diatoms-From Cell Wall Biogenesis to Nanotechnology. Annu. Rev. Genet. 2008, 42 (1), 83-107.
- (7) Kroger, N.; Deutzmann, R.; Bergsdorf, C.; Sumper, M. Species-Specific Polyamines from Diatoms Control Silica Morphology. Proc. Natl. Acad. Sci. U. S. A. 2000, 97 (26), 14133-14138.

- (8) Sumper, M.; Kröger, N. Silica Formation in Diatoms: The Function of Long-Chain Polyamines and Silaffins. J. Mater. Chem. 2004, 14, 2059-2065.
- (9) Kröger, N.; Lorenz, S.; Brunner, E.; Sumper, M. Self-Assembly of Highly Phosphorylated Silaffins and Their Function in Biosilica Morphogenesis. Science (Washington, DC, U. S.) 2002, 298 (5593), 584-586.
- (10) Kröger, N.; Deutzmann, R.; Sumper, M. Polycationic Peptides from Diatom Biosilica That Direct Silica Nanosphere Formation. Science (Washington, DC, U. S.) 1999, 286 (5442), 1129-1132.
- (11) Weiner, S.; Addadi, L. Design Strategies in Mineralized Biological Materials. J. Mater. Chem. 1997, 7 (5), 689-702.
- (12) Goobes, G.; Goobes, R.; Shaw, W. J.; Gibson, J. M.; Long, J. R.; Raghunathan, V.; Schueler-Furman, O.; Popham, J. M.; Baker, D.; Campbell, C. T. The Structure, Dynamics, and Energetics of Protein Adsorption - Lessons Learned from Adsorption of Statherin to Hydroxyapatite. Magn. Reson. Chem. 2007, 45, S32-S47.
- (13) DeGrado, W.; Lear, J. Induction of Peptide Conformation at Apolar Water Interfaces. 1. A Study with Model Peptides of Defined Hydrophobic Periodicity. J. Am. Chem. Soc. 1985, 107 (10), 7684-
- (14) Masica, D. L.; Gray, J. J.; Shaw, W. J. Partial High-Resolution Structure of Phosphorylated and Non-Phosphorylated Leucine-Rich Amelogenin Protein Adsorbed to Hydroxyapatite. J. Phys. Chem. C 2011, 115, 13775-13785.
- (15) Lu, J.; Burton, S. D.; Xu, Y. S.; Buchko, G. W.; Shaw, W. J. The Flexible Structure of the K24S28 Region of Leucine-Rich Amelogenin Protein (LRAP) Bound to Apatites as a Function of Surface Type, Calcium, Mutation, and Ionic Strength. Front. Physiol. 2014, 5, 254.
- (16) Shaw, W. J. Solid-State NMR Studies of Proteins Immobilized on Inorganic Surfaces. Solid State Nucl. Magn. Reson. 2015, 70, 1-14.
- (17) Shaw, W. J.; Ferris, K.; Tarasevich, B.; Larson, J. L. The Structure and Orientation of the C-Terminus of LRAP. Biophys. J. 2008, 94, 3247-3257.
- (18) Scudeller, L. A.; Srinivasan, S.; Rossi, A. M.; Stayton, P. S.; Drobny, G. P.; Castner, D. G. Orientation and Conformation of Osteocalcin Adsorbed onto Calcium Phosphate and Silica Surfaces. Biointerphases 2017, 12 (2), No. 02D411.
- (19) Masica, D. L.; Gray, J. J.; Shaw, W. J. Partial High-Resolution Structure of Phosphorylated and Non-Phosphorylated Leucine-Rich Amelogenin Protein Adsorbed to Hydroxyapatite. J. Phys. Chem. C 2011, 115 (28), 13775-13785.
- (20) Masica, D. L.; Ash, J. T.; Ndao, M.; Drobny, G. P.; Gray, J. J. Toward a Structure Determination Method for Biomineral-Associated Protein Using Combined Solid- State NMR and Computational Structure Prediction. Structure 2010, 18 (12), 1678-1687.
- (21) Gibson, J. M.; Popham, J. M.; Raghunathan, V.; Stayton, P. S.; Drobny, G. P. A Solid-State NMR Study of the Dynamics and Interactions of Phenylalanine Rings in a Statherin Fragment Bound to Hydroxyapatite Crystals. J. Am. Chem. Soc. 2006, 128 (16), 5364-5370.
- (22) Gibson, J. M.; Raghunathan, V.; Popham, J. M.; Stayton, P. S.; Drobny, G. P. A REDOR NMR Study of a Phosphorylated Statherin Fragment Bound to Hydroxyapatite Crystals. J. Am. Chem. Soc. 2005, 127 (26), 9350-9351.
- (23) Makrodimitris, K.; Masica, D. L.; Kim, E. T.; Gray, J. J. Structure Prediction of Protein-Solid Surface Interactions Reveals a Molecular Recognition Motif of Statherin for Hydroxyapatite. J. Am. Chem. Soc. 2007, 129 (44), 13713-13722.
- (24) Ndao, M.; Ash, J. T.; Breen, N. F.; Goobes, G.; Stayton, P. S.; Drobny, G. P. A 13C{ 31P} REDOR NMR Investigation of the Role of Glutamic Acid Residues in Statherin- Hydroxyapatite Recognition. Langmuir 2009, 25 (20), 12136-12143.
- (25) Weidner, T.; Dubey, M.; Breen, N. F.; Ash, J.; Baio, J. E.; Jaye, C.; Fischer, D. A.; Drobny, G. P.; Castner, D. G. Direct Observation of Phenylalanine Orientations in Statherin Bound to Hydroxyapatite Surfaces. J. Am. Chem. Soc. 2012, 134 (21), 8750-8753.
- (26) Weidner, T.; Breen, N. F.; Li, K.; Drobny, G. P.; Castner, D. G. Sum Frequency Generation and Solid-State NMR Study of the

- Structure, Orientation, and Dynamics of Polystyrene-Adsorbed Peptides. Proc. Natl. Acad. Sci. U. S. A. 2010, 107 (30), 13288-13293.
- (27) Ndao, M.; Ash, J. T.; Stayton, P. S.; Drobny, G. P. The Role of Basic Amino Acids in the Molecular Recognition of Hydroxyapatite by Statherin Using Solid State NMR. Surf. Sci. 2010, 604 (15-16), L39-L42.
- (28) Li, K.; Emani, P. S.; Ash, J.; Groves, M.; Drobny, G. P. A Study of Phenylalanine Side-Chain Dynamics in Surface-Adsorbed Peptides Using Solid-State Deuterium NMR and Rotamer Library Statistics. J. Am. Chem. Soc. 2014, 136 (32), 11402-11411.
- (29) Brandt, E. G.; Lyubartsev, A. P. Molecular Dynamics Simulations of Adsorption of Amino Acid Side Chain Analogues and a Titanium Binding Peptide on the TiO 2 (100) Surface. J. Phys. Chem. C 2015, 119 (32), 18126-18139.
- (30) Goobes, R.; Goobes, G.; Shaw, W. J.; Drobny, G. P.; Campbell, C. T.; Stayton, P. S. Thermodynamic Roles of Basic Amino Acids in Statherin Recognition of Hydroxyapatite. Biochemistry 2007, 46 (16), 4725-4733.
- (31) Makrodimitris, K.; Masica, D. L.; Kim, E. T.; Gray, J. J. Structure Prediction of Protein-Solid Surface Interactions Reveals a Molecular Recognition Motif of Statherin for Hydroxyapatite. J. Am. Chem. Soc. 2007, 129 (44), 13713-13722.
- (32) Weidner, T.; Dubey, M.; Breen, N. F.; Ash, J.; Baio, J. E.; Jaye, C.; Fischer, D. A.; Drobny, G. P.; Castner, D. G. Direct Observation of Phenylalanine Orientations in Statherin Bound to Hydroxyapatite Surfaces. J. Am. Chem. Soc. 2012, 134, 8750-8753.
- (33) Raj, P. A.; Johnsson, M.; Levine, M. J.; Nancollas, G. H. Salivary Statherin: Dependence on Sequence, Charge, Hydrogen Bonding Potency, and Helical Conformation for Adsorption to Hydroxyapatite and Inhibition of Mineralization. J. Biol. Chem. 1992, 267 (9), 5968-5976.
- (34) Goobes, G.; Goobes, R.; Schueler-Furman, O.; Baker, D.; Stayton, P. S.; Drobny, G. P. Folding of the C-Terminal Bacterial Binding Domain in Statherin upon Adsorption onto Hydroxyapatite Crystals. Proc. Natl. Acad. Sci. U. S. A. 2006, 103 (44), 16083-16088.
- (35) Long, J. R.; Shaw, W. J.; Stayton, P. S.; Drobny, G. P. Structure and Dynamics of Hydrated Statherin on Hydroxyapatite as Determined by Solid-State NMR. Biochemistry 2001, 40 (51), 15451-15455.
- (36) Moreno, E. C.; Kresak, M.; Hay, D. I. Adsorption of Molecules of Biological Interest onto Hydroxyapatite. Calcif. Tissue Int. 1984, 36 (1), 48-59.
- (37) Elgavish, G. A.; Hay, D. I.; Schlesinger, D. H. 1H and 31P Nuclear Magnetic Resonance Studies of Human Salivary Statherin. Int. J. Pept. Protein Res. 1984, 23 (3), 230-234.
- (38) Naganagowda, G. A.; Gururaja, T. L.; Levine, M. J. Delineation of Conformational Preferences in Human Salivary Statherin By1H,31P NMR and CD Studies: Sequential Assignment and Structure-Function Correlations. J. Biomol. Struct. Dyn. 1998, 16 (1), 91-107.
- (39) Roehrich, A.; Drobny, G. P. Solid-State NMR Studies of Biomineralization Peptides and Proteins. Acc. Chem. Res. 2013, 46 (9), 2136-2144.
- (40) Raghunathan, V.; Gibson, J. M.; Goobes, G.; Popham, J. M.; Louie, E. A.; Stayton, P. S.; Drobny, G. P. Homonuclear and Heteronuclear NMR Studies of a Statherin Fragment Bound to Hydroxyapatite Crystals. J. Phys. Chem. B 2006, 110 (18), 9324-9332.
- (41) Douglas, W. H.; Reeh, E. S.; Ramasubbu, N.; Raj, P. A.; Bhandary, K. K.; Levine, M. J. Statherin: A Major Boundary Lubricant of Human Saliva. Biochem. Biophys. Res. Commun. 1991, 180 (1), 91-
- (42) Shaw, W. J.; Long, J. R.; Campbell, A. A.; Stayton, P. S.; Drobny, G. P. A Solid State NMR Study of Dynamics in a Hydrated Salivary Peptide Adsorbed to Hydroxyapatite [3]. J. Am. Chem. Soc. **2000**, *122*, *7118*–*7119*.
- (43) Shaw, W. J.; Long, J. R.; Dindot, J. L.; Campbell, A. A.; Stayton, P. S.; Drobny, G. P. Determination of Statherin N-Terminal Peptide

- Conformation on Hydroxyapatite Crystals. J. Am. Chem. Soc. 2000, 122 (8), 1709–1716.
- (44) Masica, D. L.; Gray, J. J. Solution- and Adsorbed-State Structural Ensembles Predicted for the Statherin-Hydroxyapatite System. *Biophys. J.* **2009**, *96* (8), 3082–3091.
- (45) Goobes, G.; Goobes, R.; Schueler-Furman, O.; Baker, D.; Stayton, P. S.; Drobny, G. P. Folding of the C-Terminal Bacterial Binding Domain in Statherin upon Adsorption onto Hydroxyapatite Crystals. *Proc. Natl. Acad. Sci. U. S. A.* **2006**, *103* (44), 16083–16088.
- (46) Valsson, O.; Tiwary, P.; Parrinello, M. Enhancing Important Fluctuations: Rare Events and Metadynamics from a Conceptual Viewpoint. *Annu. Rev. Phys. Chem.* **2016**, *67* (1), 159–184.
- (47) Laio, A.; Parrinello, M. Escaping Free-Energy Minima. *Proc. Natl. Acad. Sci. U. S. A.* **2002**, 99 (20), 12562–12566.
- (48) Deighan, M.; Pfaendtner, J. Exhaustively Sampling Peptide Adsorption with Metadynamics. *Langmuir* **2013**, 29 (25), 7999–8009
- (49) Neal, S.; Nip, A. M.; Zhang, H.; Wishart, D. S. Rapid and Accurate Calculation of Protein 1H, 13C and 15N Chemical Shifts. *J. Biomol. NMR* **2003**, 26 (3), 215–240.
- (50) Kohlhoff, K. J.; Robustelli, P.; Cavalli, A.; Salvatella, X.; Vendruscolo, M. Fast and Accurate Predictions of Protein NMR Chemical Shifts from Interatomic Distances. *J. Am. Chem. Soc.* **2009**, *131* (39), 13894–13895.
- (51) Bonomi, M.; Camilloni, C.; Vendruscolo, M. Metadynamic Metainference: Enhanced Sampling of the Metainference Ensemble Using Metadynamics. *Sci. Rep.* **2016**, 6 (1), 31232.
- (52) Bonomi, M.; Camilloni, C.; Cavalli, A.; Vendruscolo, M. Metainference: A Bayesian Inference Method for Heterogeneous Systems. *Sci. Adv.* **2016**, 2 (1), No. e1501177.
- (53) Bonomi, M.; Camilloni, C. Integrative Structural and Dynamical Biology with PLUMED-ISDB. *Bioinformatics* **2017**, 33 (24), 3999–4000.
- (54) Raiteri, P.; Laio, A.; Gervasio, F. L.; Micheletti, C.; Parrinello, M. Efficient Reconstruction of Complex Free Energy Landscapes by Multiple Walkers Metadynamics. *J. Phys. Chem. B* **2006**, *110* (8), 3533–3539
- (55) Shen, Y.; Bax, A. Protein Backbone and Sidechain Torsion Angles Predicted from NMR Chemical Shifts Using Artificial Neural Networks. *J. Biomol. NMR* **2013**, *56* (3), 227–241.
- (56) Robustelli, P.; Kohlhoff, K.; Cavalli, A.; Vendruscolo, M. Using NMR Chemical Shifts as Structural Restraints in Molecular Dynamics Simulations of Proteins. *Structure* **2010**, *18* (8), 923–933.
- (57) Boehr, D. D.; Nussinov, R.; Wright, P. E. The Role of Dynamic Conformational Ensembles in Biomolecular Recognition. *Nat. Chem. Biol.* **2009**, *5*, 789–796.
- (58) Fernandez, V. L.; Reimer, J. A.; Denn, M. M. Magnetic Resonance Studies of Polypeptides Adsorbed on Silica and Hydroxyapatite Surface. *J. Am. Chem. Soc.* **1992**, *114*, 9634–9642.
- (59) Shen, Y.; Bax, A. Protein Backbone and Sidechain Torsion Angles Predicted from NMR Chemical Shifts Using Artificial Neural Networks. *J. Biomol. NMR* **2013**, *56* (3), 227–241.
- (60) Pettersen, E. F.; Goddard, T. D.; Huang, C. C.; Couch, G. S.; Greenblatt, D. M.; Meng, E. C.; Ferrin, T. E. UCSF Chimera A Visualization System for Exploratory Research and Analysis. *J. Comput. Chem.* **2004**, 25 (13), 1605–1612.
- (61) Koutsopoulos, S.; Dalas, E. Inhibition of Hydroxyapatite Formation in Aqueous Solutions by Amino Acids with Hydrophobic Side Groups. *Langmuir* **2000**, *16* (16), 6739–6744.
- (62) Buckle, E. L.; Lum, J. S.; Roehrich, A.; Stote, R. E.; Dracinsky, M.; Filocamo, S. F.; Vandermoon, B.; Drobny, G. P. Serine-Lysine Peptides as Mediators for the Production of Titanium Dioxide: Effects of Primary Structure and Secondary Structure Investigated Using Solid-State NMR Spectroscopy and DFT Calculations. *J. Phys. Chem. B* **2018**, *122*, 4708.
- (63) Chen, P.-H.; Tseng, Y.-H.; Mou, Y.; Tsai, Y.-L.; Guo, S.-M.; Huang, S.-J.; Yu, S. S.-F.; Chan, J. C. C. Adsorption of a Statherin Peptide Fragment on the Surface of Nanocrystallites of Hydroxyapatite. *J. Am. Chem. Soc.* **2008**, *130* (9), 2862–2868.

- (64) Santos, O.; Kosoric, J.; Hector, M. P.; Anderson, P.; Lindh, L. Adsorption Behavior of Statherin and a Statherin Peptide onto Hydroxyapatite and Silica Surfaces by in Situ Ellipsometry. *J. Colloid Interface Sci.* **2008**, 318 (2), 175–182.
- (65) Wilson, C. J.; Clegg, R. E.; Leavesley, D. I.; Pearcy, M. J. Mediation of Biomaterial—Cell Interactions by Adsorbed Proteins: A Review. *Tissue Eng.* **2005**, *11* (1–2), 1–18.
- (66) Jones, F. H. Teeth and Bones: Applications of Surface Science to Dental Materials and Related Biomaterials. *Surf. Sci. Rep.* **2001**, 42 (3–5), 75–205.
- (67) MacDonald, D. E.; Deo, N.; Markovic, B.; Stranick, M.; Somasundaran, P. Adsorption and Dissolution Behavior of Human Plasma Fibronectin on Thermally and Chemically Modified Titanium Dioxide Particles. *Biomaterials* **2002**, 23 (4), 1269–1279.
- (68) Verket, A.; Tiainen, H.; Haugen, H. J.; Lyngstadaas, S. P.; Nilsen, O.; Reseland, J. E. Enhanced Osteoblast Differentiation on Scaffolds Coated with TiO 2 Compared to SiO 2 and CaP Coatings. *Biointerphases* **2012**, 7 (1–4), 36.
- (69) Morcombe, C. R.; Zilm, K. W. Chemical Shift Referencing in MAS Solid State NMR. J. Magn. Reson. 2003, 162 (2), 479–486.
- (70) Bertani, P.; Raya, J.; Bechinger, B. 15N Chemical Shift Referencing in Solid State NMR. *Solid State Nucl. Magn. Reson.* **2014**, 61–62, 15–18.
- (71) Lindorff-Larsen, K.; Piana, S.; Palmo, K.; Maragakis, P.; Klepeis, J. L.; Dror, R. O.; Shaw, D. E. Improved Side-Chain Torsion Potentials for the Amber Ff99SB Protein Force Field. *Proteins: Struct., Funct., Genet.* **2010**, 78 (8), NA–NA.
- (72) Perera, L.; Berkowitz, M. L. Many-Body Effects in Molecular Dynamics Simulations of Na+(H2O)n and Cl-(H2O)n Clusters. *J. Chem. Phys.* **1991**, 95 (3), 1954.
- (73) Heinz, H.; Lin, T.-J.; Kishore Mishra, R.; Emami, F. S. Thermodynamically Consistent Force Fields for the Assembly of Inorganic, Organic, and Biological Nanostructures: The INTERFACE Force Field. *Langmuir* **2013**, 29 (6), 1754–1765.
- (74) Předota, M.; Bandura, A. V.; Cummings, P. T.; Kubicki, J. D.; Wesolowski, D. J.; Chialvo, A. A.; Machesky, M. L. Electric Double Layer at the Rutile (110) Surface. 1. Structure of Surfaces and Interfacial Water from Molecular Dynamics by Use of Ab Initio Potentials. *J. Phys. Chem. B* **2004**, *108* (32), 12049–12060.
- (75) Sprenger, K. G.; Prakash, A.; Drobny, G.; Pfaendtner, J. Investigating the Role of Phosphorylation in the Binding of Silaffin Peptide R5 to Silica with Molecular Dynamics Simulations. *Langmuir* **2018**, *34* (3), 1199–1207.
- (76) Prakash, A.; Sprenger, K. G.; Pfaendtner, J. Essential Slow Degrees of Freedom in Protein-Surface Simulations: A Metadynamics Investigation. *Biochem. Biophys. Res. Commun.* **2018**, 498 (2), 274–281.
- (77) Emami, F. S.; Puddu, V.; Berry, R. J.; Varshney, V.; Patwardhan, S. V.; Perry, C. C.; Heinz, H. Prediction of Specific Biomolecule Adsorption on Silica Surfaces as a Function of PH and Particle Size. *Chem. Mater.* **2014**, 26 (19), 5725–5734.
- (78) Heinz, H. Adsorption of Biomolecules and Polymers on Silicates, Glasses, and Oxides: Mechanisms, Predictions, and Opportunities by Molecular Simulation. *Curr. Opin. Chem. Eng.* **2016**, *11*, 34–41.
- (79) Wu, C.; Chen, M.; Xing, C. Molecular Understanding of Conformational Dynamics of a Fibronectin Module on Rutile (110) Surface. *Langmuir* **2010**, 26 (20), 15972–15981.
- (80) Berendsen, H. J. C.; Postma, J. P. M.; Van Gunsteren, W. F.; Dinola, A.; Haak, J. R. Molecular Dynamics with Coupling to an External Bath. *J. Chem. Phys.* **1984**, *81* (8), 3684–3690.
- (81) Bussi, G.; Donadio, D.; Parrinello, M. Canonical Sampling through Velocity Rescaling. J. Chem. Phys. 2007, 126 (1), No. 014101.
- (82) Darden, T.; York, D.; Pedersen, L. Particle Mesh Ewald: An $N \cdot \log(N)$ Method for Ewald Sums in Large Systems. *J. Chem. Phys.* **1993**, 98 (12), 10089–10092.
- (83) Hess, B.; Bekker, H.; Berendsen, H. J. C.; Fraaije, J. G. E. M. LINCS: A Linear Constraint Solver for Molecular Simulations. *J. Comput. Chem.* **1997**, *18* (12), 1463–1472.

- (84) Abraham, M. J.; Murtola, T.; Schulz, R.; Páll, S.; Smith, J. C.; Hess, B.; Lindahl, E. Gromacs: High Performance Molecular Simulations through Multi-Level Parallelism from Laptops to Supercomputers. *SoftwareX* **2015**, *1*–2, 19–25.
- (85) Pfaendtner, J.; Bonomi, M. Efficient Sampling of High-Dimensional Free-Energy Landscapes with Parallel Bias Metadynamics. J. Chem. Theory Comput. 2015, 11 (11), 5062–5067.
- (86) Hornak, V.; Abel, R.; Okur, A.; Strockbine, B.; Roitberg, A.; Simmerling, C. Comparison of Multiple Amber Force Fields and Development of Improved Protein Backbone Parameters. *Proteins: Struct., Funct., Genet.* **2006**, *65* (3), 712–725.
- (87) Tribello, G. A.; Bonomi, M.; Branduardi, D.; Camilloni, C.; Bussi, G. PLUMED 2: New Feathers for an Old Bird. *Comput. Phys. Commun.* **2014**, *185* (2), 604–613.
- (88) Prakash, A.; Fu, C. D.; Bonomi, M.; Pfaendtner, J. Biasing Smarter, Not Harder, By Partitioning Collective Variables Into Families. *J. Chem. Theory Comput.* **2018**, *14*, 4985–4990.
- (89) Torrie, G. M.; Valleau, J. P. Nonphysical Sampling Distributions in Monte Carlo Free-Energy Estimation: Umbrella Sampling. *J. Comput. Phys.* **1977**, 23 (2), 187–199.
- (90) Daura, X.; Gademann, K.; Jaun, B.; Seebach, D.; van Gunsteren, W. F.; Mark, A. E. Peptide Folding: When Simulation Meets Experiment. *Angew. Chem., Int. Ed.* **1999**, 38 (1–2), 236–240.